C. R. Mecanique 343 (2015) 344–353

Contents lists available at ScienceDirect

Comptes Rendus Mecanique

www.sciencedirect.com

Investigation of indentation-, impact- and scratch-induced mechanically affected zones in a copper single crystal

Pierre Juran [b], Pierre-Jacques Liotier [b], Claire Maurice [b], Frédéric Valiorgue [a], Guillaume Kermouche [b,*]

[a] Université de Lyon, École nationale d'ingénieurs de Saint-Étienne, Laboratoire de tribologie et dynamique des systèmes, UMR 5513 CNRS/ECL/ENISE, 58 rue Jean-Parot, 42023 Saint-Étienne cedex 2, France
[b] École des mines de Saint-Étienne, Centre SMS, Laboratoire LGF UMR CNRS 5307, 158, cours Fauriel, 42023 Saint-Étienne cedex 2, France

ARTICLE INFO

Article history:
Received 23 December 2014
Accepted after revision 23 March 2015
Available online 29 April 2015

Keywords:
Indentation
Scratch
Micro-impact
EBSD
Crystal plasticity
Finite-element analysis
Surface mechanical treatment
Lattice misorientation

ABSTRACT

Many nanomechanical testings and surface mechanical treatments—burnishing, shot peening...—are based upon contact phenomena such as indentation, impact and scratch loadings. In this paper, the Mechanically Affected Zone (MAZ) induced by these standard contact loadings applied on a single crystal copper is investigated. We assume that the MAZ can be characterized by the lattice misorientation measured using backscattering electron diffraction. With the help of a Finite-Element analysis, it is shown that crystal plasticity theory can estimate with enough accuracy the lattice misorientation pattern. Experimental results highlight that the MAZ size is always related to the residual imprint dimension and its shape depends strongly on the kind of loading.

1. Introduction

Indentation, scratch and impact loadings are standard contact phenomena commonly used to characterize the mechanical properties of materials at the micro or nanoscale. Instrumented indentation testing is the most popular technique to determine local quasi-static mechanical properties [1–4]. Standard indentation testing is unfortunately unable to identify high strain-rate-dependent mechanical properties, and in this case, impact-based methods such as dynamic indentation or micro-impact testing [5–7] are more adequate. Identification of medium-to-large-strain mechanical properties is out of the scope of indentation and impact-based testing. For the medium strain range, microcompression testing is an available solution, but the fabrication of the micro-pillars and the running of the tests are expensive, time-consuming and require special care [8–10]. Scratch tests are a promising alternative because of the large strains induced in the near-surface without requiring specific cares to the test procedure [11–13]. Nevertheless, indentation, impact and scratch are non-homogeneous loadings and thus the relation with the sample stress–strain curves is not explicit. There is still today numerous works dealing with this topic [14–16], showing the need to better understand the responses of materials under such kinds of loading.

Indentation, scratch and impact loading types are also involved in many surface mechanical treatments. Surface treatments are usually connected with the modification of the surface properties by various actions of physical, chemical, thermal or metallurgical origin (quenching, nitriding...). However, mechanical loading may also result in modifications such as the

* Corresponding author. Tel.: +33(0)4 77 42 00 74
E-mail address: kermouche@emse.fr (G. Kermouche).

http://dx.doi.org/10.1016/j.crme.2015.03.003
1631-0721/

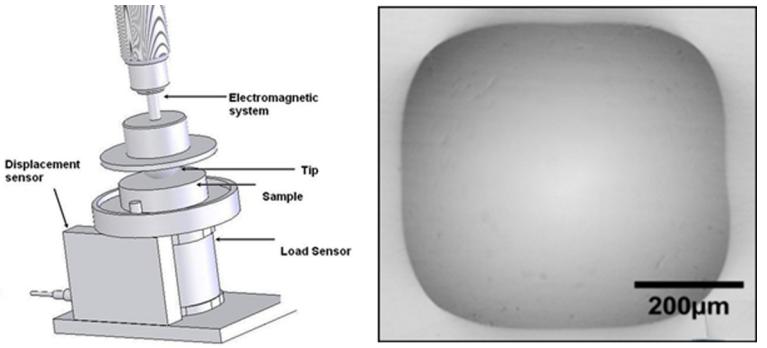

Fig. 1. Left: micro-impact set up [7], right: residual indent imprint resulting from a Brinell test (2.5 mm, 100 N) on a single-crystal copper surface ({100} face). The square-shaped imprint (not shown here) is also observed under impact loading and is a consequence of the single crystal anisotropic plastic flow.

creation of compressive residual stress fields [17–19] or refinement of the micro-structure [20,21] without any thermal or chemical phenomena. We distinguish treatments based on normal or quasi-normal contacts (like indentation, impact) such as shot peening [22–26] or hammering, and treatments based on tangential contacts (like scratching) such as burnishing [27–29] and polishing [30,31]. The understanding of the response to such contact loading types in terms of residual stress or in terms of induced microstructure changes is of primary importance in the context of the optimization of surface mechanical treatments.

This paper aims at characterizing and comparing the shape and the size of the Mechanically Affected Zone (MAZ) induced by indentation, impact and scratch loadings. The MAZ corresponds to the zone in which the microstructure was altered by the mechanical treatment. This concept defined in the present paper has been inspired from the well-known Heat Affected Zone (HAZ) induced by welding processes [32] or the Thermo-Mechanically Affected Zone (TMAZ) induced by friction stir welding processes [33]. One important issue is to find a reliable method to characterize the MAZ in such processes. For instance, the MAZ could correspond to the zone where severe plastic deformation occurs under repeated contact [34–38]. Nevertheless, this definition is not able to take into account the residual stress field zone [18], this last being also a consequence of small plastic deformation, not detectable by means of standard metallurgical characterization methods. In this paper, we propose to investigate the MAZ by means of the lattice misorientation measured using backscattering electron diffraction [39]. The drawback of this approach is that it is quantitative only if it is used on a single grain with no initial misorientation. This is the reason why we investigated the effect of these different loadings on a copper single crystal.

First, the sample preparation and experimental set-up are presented. A physically-motivated Crystal Plasticity Finite-Element Model (CPFEM) based on the works of Kubin et al. [40–42] is then detailed. Comparison of the CPFEM and the experimental lattice misorientation field is conducted for indentation loading over the cross-section of the residual print. It is then extended to the analyses of impact and scratch-induced lattice misorientation field, using the same contact geometry—i.e. equivalent ratio contact radius over ball radius. The difference between these three kinds of loading is then discussed in terms of size and shape of the resulting MAZ.

2. Materials and methods

A copper single crystal was produced by directional solidification using a standard zone melting method based on a horizontal Bridgman-type apparatus. The indented, impacted and scratched surfaces were {100}, oriented along the direction of the surface normal.

The indents were carried out using a standard Brinell Hardness set-up. The ball diameter is 2.5 mm and the maximum indentation load used was 100 N. Because of the anisotropic plastic flow of fcc single crystals, the resulting imprint is square-shaped as expected [43–46]. In the sequel of this paper, the term *imprint diameter* will refer to the side length of the square in order to be consistent with the literature about indentation testing.

The impacts were performed using the micro-impact set-up detailed in previous studies [16,7]. This device allows one to measure with high accuracy the impact speed and thus the impact energy (Fig. 1). The equivalent impact strain rate could be estimated as being proportional to the ratio between impact speed and contact radius. In the present investigation, the ball diameter is 2 mm, the impact speed was set to 100 $\mathrm{mm\,s^{-1}}$. The resulting equivalent strain rate was estimated to be close to 100 $\mathrm{s^{-1}}$ using the relation proposed by Mok et al. [5]. Note that the imprint was also observed to be square-shaped similarly to static ball indentation.

Scratches were produced in a Hermle C800 machining center using an Ecoroll roller burnishing system 2, composed of a high-pressure hydraulic pump and a roller burnishing tool with a 6-mm-diameter ceramic ball. Similarly to impact testing, the equivalent strain rate could be approximated by the ratio between sliding speed and contact length. The scratching speed was set to 15 $\mathrm{mm\,s^{-1}}$ and the resulting equivalent strain rate was estimated at 20 $\mathrm{s^{-1}}$ using the residual groove width (Fig. 2).

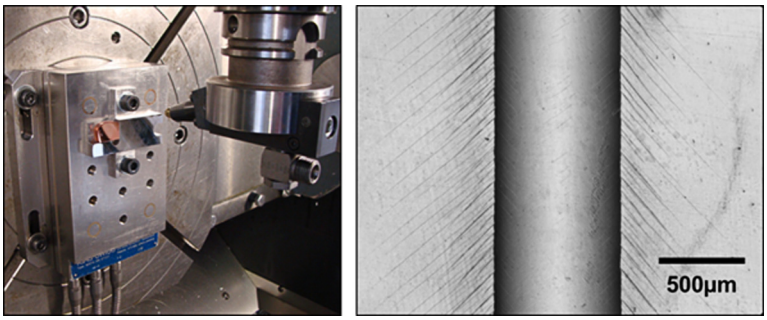

Fig. 2. (Color online.) Left: burnishing set-up used to perform the scratch test, right: scratch-induced residual groove left by a spherical tip 6 mm in diameter on a single-crystal copper surface ({100} face).

It is commonly assumed that the deformation level under scratch or indentation loadings with a spherical tip is proportional to the contact severity defined as:

$$\varepsilon_r \propto \frac{a}{R} \tag{1}$$

where a is the contact radius and R is the ball radius. In this work, the elastic deformation can be neglected. The contact radius is therefore equivalent to the imprint radius. For each kind of loading type, the process conditions have been chosen to lead to the same contact severity ($\frac{a}{R} \approx 0.2$).

The samples were cut by EDM (Electric Discharge Machining) and were then polished. As shown by Liu et al. [47], mechanical polishing of a copper single crystal may create a thin deformed layer up to 1 µm. This is the reason why a final step of electro-polishing was performed.

EBSD measurements over the resulting cross-sections were performed using a using a Zeiss Supra 55 VPFEG-SEM operated at 20 kV with a probe current of 2 nA. EBSD analyses were carried out using an HKL system (now Oxford Instruments) composed of a NordlysII camera and the Channel 5 software suite.

3. 3D Finite-Element modelling of spherical indentation

A physically-motivated Crystal Plasticity Finite-Element Model (CPFEM) based on the works of Kubin et al. [40–42] is detailed in this section. Simulations were performed using the commercial ABAQUS Finite-Element software [48], where the constitutive model was implemented through a UMAT subroutine.

3.1. Crystal plasticity model

Similarly to most of crystal plasticity models [41,44,45,49], the constitutive model used in this paper is based on the expanded Taylor relation [50].

$$\tau_c^i = \mu\, b \sqrt{\sum_j a_{ij} \rho^j} \tag{2}$$

In this equation μ is the shear modulus, b is the magnitude of the Burgers vector of the dislocations, τ_c^i is the critical stress for the activation of the slip system (i), which is determined by dislocation densities ρ^j in all slip systems (j) including (i) itself. The matrix a_{ij} is defined such that $\sqrt{a_{ij}}$ represents the average strength of the interaction between the two slip systems (i) and (j).

Those coefficients are related to local and non-local effects of the line tension due to the forest dislocation density ρ_f [40,41]. A correction is applied to the a_{ij} coefficients due to interactions between dislocation junctions (Hirth, Lomer, Glissile) if the dislocation density is different from the reference value ρ_{ref} used for their determination by dislocation dynamics simulations. Devincre et al. [40] have proved that the modifications to apply to the coefficients of the interaction matrix can be computed from Eq. (3).

$$\sqrt{a_{ij}} = \frac{\ln\left(\frac{1}{(b\sqrt{a_{ref}\rho_f})}\right)}{\ln\left(\frac{1}{(b\sqrt{a_{ref}\rho_{ref}})}\right)} \sqrt{a_{ij,ref}} \tag{3}$$

where a_{ref} is set to 0.35 according to Madec et al. [51]. Note that the $a_{ij,ref}$ coefficients have been calculated for $\rho_{ref} = 1\ \mu m^{-2}$ [40].

When the local resolved stress overpasses the critical stress τ_c^i for the considered slip system, a non-null plastic strain γ^i appears and its dislocation density increases since the amount of stored dislocations rises in this slip system. As most of crystal plasticity models [52,44,49], a strain-rate-dependent framework is used. The plastic flow is thus described by Eq. (4).

Table 1
Constitutive model parameters [41].

μ	Shear modulus	42 GPa
b	Burgers vector	$2.57{\cdot}10^{-10}$ m^{-2}
$\dot{\gamma}_0$	Reference shear strain for the flow law	10^{-3} s^{-1}
n	Exponent for the flow law	50
a'_0	Self interaction coefficient	0.122
a_{copla}	coplanar interaction coefficient	0.122
a_{ortho}	Hirth interaction coefficient at ρ_{ref}	0.07
a_{col}	Colinear interaction coefficient at ρ_{ref}	0.625
a_2	Glissile interaction coefficient at ρ_{ref}	0.137
a_3	Lomer interaction coefficient at ρ_{ref}	0.122
K_{I}	Mean free path for self-interactions	180
K_{copla}	Mean free path for coplanar interactions	180
K_{junct}	Mean free path for junction interactions	5–10

$$\dot{\gamma}^i = \dot{\gamma}_0 \left| \frac{\tau^i}{\tau_c^i} \right|^n \operatorname{sgn}(\tau^i) \tag{4}$$

The strain hardening can be expressed as a matrix h_{ij} describing the interactions between the systems i and j.

$$\dot{\tau_c}^i = \sum_j h_{ij} \left| \dot{\gamma}^i \right| \tag{5}$$

Coefficients h_{ij} can be obtained from Eqs. (5) and (2).

According to Kubin et al. [41], the total dislocation storage rate is obtained by summing individual storage rates or the inverses of related mean free paths:

$$\frac{\mathrm{d}\rho^i}{\mathrm{d}\gamma^i} = \frac{1}{b} \left(\frac{\sqrt{a'_0 \rho^i}}{K_{\text{I}}} + \frac{\sum_{j \in \text{copla}(i)} \sqrt{a_{\text{copla}} \rho^j}}{K_{\text{copla}}} + \frac{\sqrt{\sum_{k \neq i \neq j} a_{ik} \rho^k}}{K_{\text{junct}}} \right) \tag{6}$$

where K_{I} denotes the mean free path constant for self-interactions, a'_0 is the self interaction coefficient, K_{copla} denotes the mean free path constant for coplanar interactions and a_{copla} is the coplanar interaction coefficient, K_{junct} is the mean free path constant describing the formation of junctions.

The first term at the right-hand side describes the self-interaction. The second term account for coplanar interactions. It includes a summation since a slip system has two possible coplanar slip systems in the fcc structure. The third term is the contribution from the three junction-forming interactions (Hirth, Lomer, and Glissile). The parameters of the present constitutive model are given in Table 1 and the interaction matrix can be found in [51,40]. Note that the only adjustable parameter is the initial dislocation density ρ_0 per slip system, which is a consequence of the sample fabrication process.

Although some studies have demonstrated the interest of considering dynamic recovering [42,49], it has been neglected in the present investigation. Therefore, the present model is not built to account accurately for stage 4 of work-hardening. This is the reason why the chosen indentation depth is small enough to avoid deformation levels larger than the one required to activate this hardening stage. More precisely, the total plastic strain at maximum indentation load does not exceed 0.11 and is lower than 0.06 in the region where lattice misorientation is maximum.

3.2. Mesh and boundary conditions

The numerical simulations are performed using a large displacement/large strain formulation—updated Lagrangian [53]. The constitutive model, which has been detailed in this paper using a small transformation hypothesis for clarity, has been extended to finite deformation using the multiplicative decomposition of the deformation gradient into an elastic and a plastic part and the Jauman objective stress rate [54]. An implicit FE scheme is used. The indenter is a rigid sphere. The contact between the indenter and the surface is assumed as frictionless and is treated using the augmented Lagrangian method. The loading is achieved by adjusting the quasi-static displacement of the indenter which is pushed down vertically (z-axis) into the specimen. The Finite-Element domain is a right-angled parallelepiped. Because of the crystal orientation and of the loading direction, planes ($x = 0$) and ($y = 0$) are planes of symmetry. The Finite-Element domain is a right-angled parallelepiped shown in Fig. 3. The mesh is constituted of 8-node-brick isoparametric elements with a selective reduced integration scheme to ensure plastic incompressibility. The average element length close to the surface is 20 microns. This size has been chosen to have more than 10 nodes in contact over a given edge.

As explained in the previous section, the only adjustable parameter of the crystal plasticity model is the initial dislocation density ρ_0 per slip system. We propose here to estimate ρ_0 by a reverse analysis of the imprint diameter–force curve (Fig. 4). An excellent agreement is observed for $\rho_0 = 3\ \mu\text{m}^{-2}$. It can also be observed in Fig. 5 that the contact area under maximum load predicted by the FEA matches experimental residual imprints. Note that the square shape is well described.

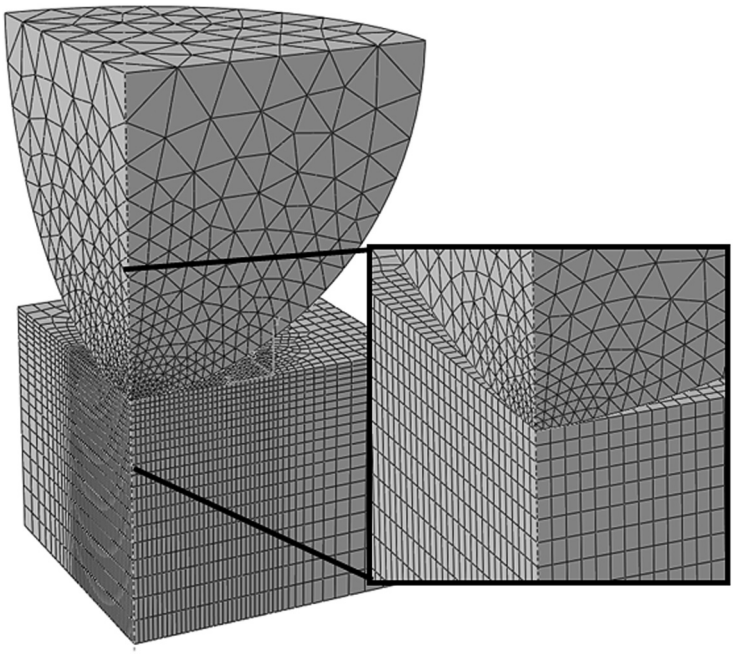

Fig. 3. Finite-Element mesh. Thanks to the crystal symmetry and the loading conditions, only a quarter of the indentation has to be meshed.

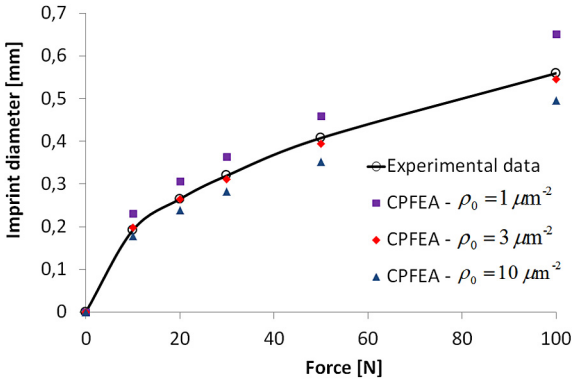

Fig. 4. (Color online.) Imprint diameter vs. indentation load. Crystal Plasticity Finite-Element calculations match the experimental data when the initial dislocation density is set to $\rho_{ref} = 3\ \mu m^{-2}$.

It points out the ability of the model to account for multiple slip system activation during spherical indentation with enough accuracy.

4. Spherical indentation results

Fig. 6 shows the indentation-induced lattice misorientation over a cross-section of the indent imprint (plane $x = 0$) for an applied load of 100 N. The misorientation is computed from the lattice orientation of a reference point taken in a zone far from the Indentation Affected Zone. The misorientation field is almost symmetric, confirming the good initial lattice orientation with respect to the indentation direction. Strongly disoriented zones appear just below the contact area perimeter, which could be linked to the pile-up caused by the incompressible plastic flow. The maximal misorientation is 7 degrees and a strong misorientation gradient is observed. It is noticeable that there was some subgrain boundaries in the single crystal before indentation. Nevertheless, EBSD maps show that their effects are not significant because there are no observable breaks in the indentation-induced misorientation field symmetry. Although the complex shape of the Mechanically Affected Zone, one may consider that it is almost fully embedded in a hemisphere having a radius close to the imprint diameter (Fig. 6). This result is consistent with the works of Alcala et al. [46]. Note that these authors define the plastic zone shape as given by the three-dimensional isocontour of the total accumulated shear strain $\gamma = 0.0005$. Nevertheless γ is not easily measurable with EBSD analysis; this is why it is likely to measure the lattice misorientation, which is also connected with the plastic flow.

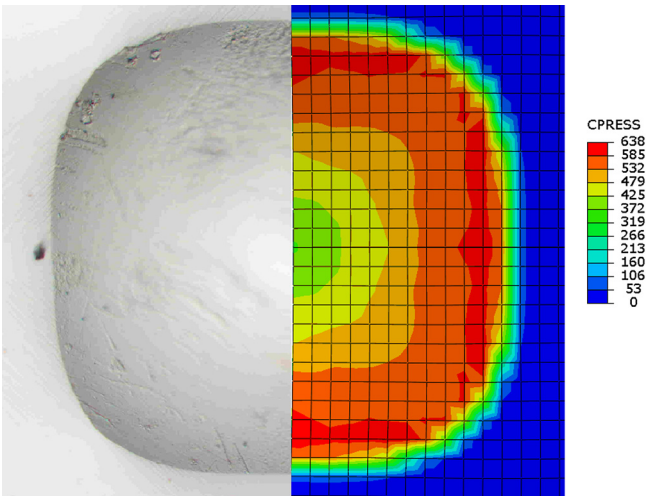

Fig. 5. (Color online.) Imprint shape ($F = 100$ N). Crystal Plasticity Finite-Element calculations match the square shape of the experimental data with good accuracy. The contact pressure distribution (CPRESS) is used here to map the contact area.

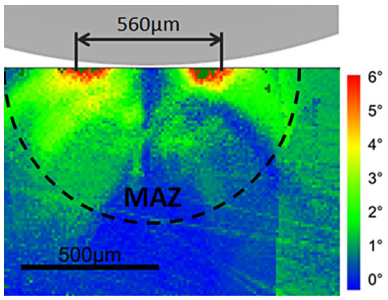

Fig. 6. (Color online.) EBSD lattice misorientation map of the indent imprint (cross-sectional view) for $F = 100$ N.

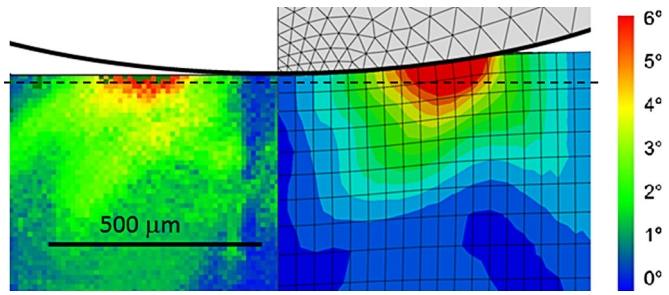

Fig. 7. (Color online.) Indentation-induced lattice misorientation (cross-sectional view) for $F = 100$ N. Left: EBSD map, right: CPFEA with initial dislocation density set to $\rho_0 = 3\ \mu m^{-2}$.

Figs. 7 and 8 show the comparison between the measured indentation-induced lattice misorientation and the misorientation resulting from the CPFEA. Note that the misorientation angle is computed in the same manner than with EBSD data post-treatment. In a few words, it is based on the comparison between current crystal orientation and the initial crystal orientation and is given by:

$$\theta = a\cos\left(\frac{\mathrm{tr}\left(\overline{\overline{P}}\right) - 1}{2}\right) \tag{7}$$

where $\overline{\overline{P}}$ is the transfer matrix from the initial crystal orientation to the current crystal orientation.

The global distribution plotted in Fig. 7 can be considered as satisfying from the point of view of the limitation of the constitutive model used. Therefore, a good agreement is observed along an horizontal path embedding the maximum lattice misorientation, as shown in Fig. 8. It thus highlights the capability of such physically-based constitutive models for describ-

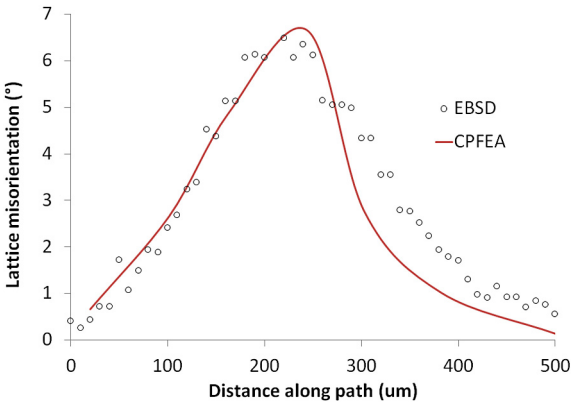

Fig. 8. (Color online.) Comparison of indentation-induced lattice misorientation for $F = 100$ N measured by EBSD and resulting from the CPFEA along the path defined by the dashed line in Fig. 7.

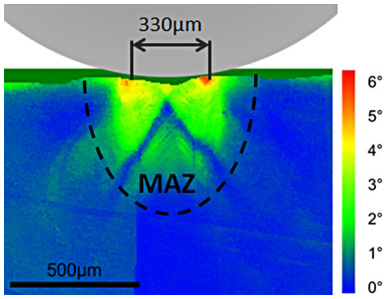

Fig. 9. (Color online.) EBSD lattice misorientation map of the impact imprint (cross-sectional view) for an impact speed set to 100 mm s^{-1} and a ball diameter of 2 mm. The resulting equivalent strain rate is roughly 100 s^{-1}.

ing fcc single-crystal indentation-induced deformation by using only one adjustable parameter—i.e. the initial dislocation density. Such a model can thus be used to understand in a more accurate way the relationship between contact conditions and the Mechanically Affected Zone. Studies dealing with the modelling of single-crystal indentation are based on comparisons with experimental data limited to the load–penetration curve or to the shape and size of the residual imprints. In the present paper, we also show that some experimental features such as lattice misorientation can be well captured if an appropriate constitutive model is used. Note, however, that the agreement would not probably be so good with horizontal lines at higher depths, which is an indication that the constitutive model could still be improved. Nevertheless indentation-induced lattice misorientation as well as the load–penetration curve may be considered as good candidates for evaluating the robustness of crystal plasticity models applied in the context on non-homogeneous loadings such as contact phenomena.

5. Impact and scratch results

Fig. 9 shows the impact-induced lattice misorientation over the cross-section of the impact imprint (plane $x = 0$). Here again, the misorientation is computed from the lattice orientation of a reference point taken in a zone far from the Mechanically Affected Zone. The misoriented area underneath the impact shares similar features with the indentation one. The misorientation field is almost symmetric, confirming the good initial lattice orientation with respect to the impact direction. The maximal misorientation is 6 degrees and a strong misorientation gradient is observed. Here again, the depth over which the lattice is disoriented is related to the imprint diameter but, contrary to the static indentation case, it is half higher than the imprint diameter. This could be interpreted as an effect of the strain rate, which plays a hardening-like role in the near-surface, and thus enhances dislocation slip in the sub-surface. It underlines therefore the need to account for a strain-rate effect in crystal plasticity constitutive models to understand impact-induced plastic deformation.

Fig. 10 shows the scratch-induced lattice misorientation over the residual groove cross-section. Here again, the orientation pattern is almost symmetric. In a similar fashion to the indentation loading case, strongly disoriented zones appear just below the contact area limits. Note however the V-shape of the orientation pattern, which is rather different than in the indentation and impact loading cases. Similarly to indentation loading, the depth of the mechanically affected zone is of the same order of magnitude than the imprint diameter. This result is in good agreement with the paper of Kermouche et al. [19], in which it is demonstrated that the depth of the scratch-induced residual stress field is close to 2–3 times the contact radius independently of the mechanical properties or the contact severity. Note that the relation of the MAZ size with the imprint radius was also mentioned in [28] for oblique impacts and scratch tests.

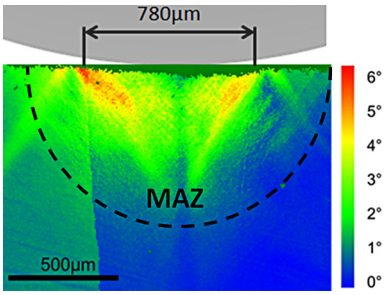

Fig. 10. (Color online.) EBSD lattice misorientation map of the scratch residual groove (cross-sectional view). The indenter is a ball of radius 3 mm. The scratching speed is 15 mm s^{-1} and the resulting equivalent strain rate is roughly 20 s^{-1}.

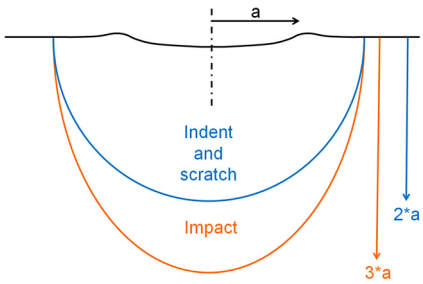

Fig. 11. (Color online.) Size and shape of the Mechanically Affected Zone induced by the different surface loadings investigated in this paper.

Here again, there was some subgrain boundaries in the single crystal before indentation. Similarly to the indentation case, it has been considered that they have a negligible influence on the crystal deformation, as the misorientation field symmetry is almost perfect after loading.

6. The Mechanically Affected Zone

The maximal distorted zone is located just under the pile-up, whatever the contact loadings—indentation, impact, or scratching. From this zone, misoriented lobes grow in various directions according to the process. For spherical indentation, these lobes spread toward the outside. For spherical impact, they grow straight under the impacted zone. For ball scratching, strongly misoriented lobes grow from the pile-up to the scratch symmetry plane. Second lobes, less distorted, spread toward the outside. Size and shape of the Mechanically Affected Zone depends on the kind of contact loading. According to Figs. 6, 9 and 10, it can be observed that the size of the MAZ is always in relation with the imprint radius a (Fig. 11).

More specifically:

- the crystal lattice is severely distorted over a depth larger than three times the contact radius in the case of the impact loading;
- indent and scratch are almost similar and modify the crystal lattice over a depth larger than two times the contact radius.

7. Conclusions

The analysis of indentation, impact and scratch loading on a single copper crystal corroborates the assumption that the Mechanically Affected Zone induced by surface mechanical treatments is always linked to the contact size [19,28]. Impact and indentation-induced lattice misorientation are almost similar, except that impacts seem to affect the material more deeply than indentation. The well-used hypothesis [11] that considers that indentation and scratch loadings affect materials in a similar way (assuming the same contact severity or deformation level) is not verified here. In both cases, the depth of the MAZ is of the order of magnitude of one time the contact diameter, but the induced lattice misorientation field over the cross section is very different. Hence the residual stress-field should also be very different. This is in good agreement with one of our previous investigations [19] showing that scratch loading may cause tensile residual stresses in the near-surface contrary to indentation or impact loadings [22].

The satisfying agreement observed in this paper between the Crystal Plasticity Finite-Element analysis and the indentation-induced lattice misorientation is promising to address the consequences of surface mechanical treatments in an academic context. Note that this model has been chosen because it was extensively used in the past for pure copper (for which constitutive parameters have been identified through the extensive use of Discrete Dislocation Dynamics) and have

shown very good agreement with tensile experiments. Other ones such as those proposed by Alcala [46] could also lead to satisfying results, but it is out of the scope of this work. Our approach could be used in a near-future to check crystal plasticity constitutive models in the context of non-homogeneous monotonous loading at low strain rate (indentation) or high strain rate (impact) and non-monotonous loadings (scratch). It appears that EBSD measurements should be an interesting way to determine new experimental data for further development of indentation-based reverse methods. Future works will also deal with the measurement of the residual stress-field induced by these loadings using HAR-EBSD [55] and with the characterization of induced MAZ in polycrystalline materials.

Acknowledgements

This work was supported by the LABEX MANUTECH-SISE (ANR-10-LABX-0075) of “Université de Lyon”, within the program “Investissements d’avenir” (ANR-11-IDEX-0007) operated by the French National Research Agency (ANR). Authors are grateful to H. Baida and C. Langlade for their contributions on micro-impact experiments and to B. Devincre and T. Hoc for fruitful discussions on fcc crystal plasticity.

References

[1] W.-C. Oliver, G. Pharr, An improved technique for determining hardness and elastic modulus using load and displacement sensing indentation experiments, J. Mater. Res. 7 (1992) 1564–1583.
[2] M. Dao, N. Chollacoop, K.-J. Van Vliet, T.-A. Ventakesh, S. Suresh, Computational modeling of the forward and reverse problems in instrumented sharp indentation, Acta Mater. 49 (2001) 3899–3918.
[3] G. Kermouche, J.L. Loubet, J.M. Bergheau, An approximate solution to the problem of cone or wedge indentation of elastoplastic solids, C. R. Mecanique 333 (5) (2005) 389–395.
[4] G. Kermouche, J.L. Loubet, J.M. Bergheau, Extraction of stress–strain curves of elastic–viscoplastic solids using conical/pyramidal indentation testing with application to polymers, Mech. Mater. 40 (2008) 271–283.
[5] C.H. Mok, J. Duffy, The dynamic stress–strain relation of metals as determined from impact tests with a hard ball, Int. J. Mech. Sci. 7 (1965) 355–371.
[6] G. Subhash, B.J. Koeppel, A. Chandra, Dynamic indentation hardness and rate sensitivity in metals, J. Eng. Mater. Technol. 121 (1999) 257–263.
[7] G. Kermouche, F. Grange, C. Langlade, Local identification of the stress–strain curves of metals at a high strain rate using repeated micro-impact testing, Mater. Sci. Eng. A. 569 (2013) 71–77.
[8] M.D. Uchic, D.M. Dimiduk, A methodology to investigate size scale effects in crystalline plasticity using uniaxial compression testing, Mater. Sci. Eng. A 400–401 (2005) 268–278.
[9] H. Zhang, B.E. Schuster, Q. Wei, K.T. Ramesh, The design of accurate micro-compression experiments, Scr. Mater. 54 (2) (2006) 181–186.
[10] R. Lacroix, G. Kermouche, J. Teisseire, E. Barthel, Plastic deformation and residual stresses in amorphous silica pillars under uniaxial loading, Acta Mater. (2012) 5555–5566.
[11] J.L. Bucaille, E. Felder, G. Hochstetter, Mechanical analysis of the scratch test on elastic and perfectly plastic materials with the three-dimensional finite element modelling, Wear 249 (2001) 422–432.
[12] M. Barge, G. Kermouche, P. Gilles, J.M. Bergheau, Experimental and numerical study of the ploughing part of abrasive wear, Wear 255 (2003) 30–37.
[13] G. Kermouche, N. Aleksy, J.L. Loubet, J.M. Bergheau, Finite element modeling of the scratch response of a coated time-dependent solid, Wear 267 (2009) 1945–1953.
[14] X. Hernot, C. Moussa, O. Bartier, Study of the concept of representative strain and constraint factor introduced by Vickers indentation, Mech. Mater. 68 (2014) 1–14.
[15] G. Kermouche, N. Aleksy, J.M. Bergheau, Viscoelastic-viscoplastic modelling of the scratch response of pmma, Adv. Mater. Sci. Eng. A (2013) 289698.
[16] C. Langlade, S. Lamri, G. Kermouche, Damage phenomena of thin hard coatings submitted to repeated impacts: influence of the substrate and film properties, Mater. Sci. Eng. A. 560 (2013) 296–305.
[17] A. Rodríguez, L.N. Lopez de Lacalle, A. Celaya, A. Lamikiz, J. Albizuri, Surface improvement of shafts by the deep ball-burnishing technique, Surf. Coat. Technol. 206 (2012) 2817–2824.
[18] S. Wang, Y. Li, M. Yao, R. Wang, Compressive residual stress introduced by shot peening, J. Mater. Process. Technol. 73 (1998) 64–73.
[19] G. Kermouche, J. Rech, H. Hamdi, J.M. Bergheau, On the residual stress field induced by a scratching round abrasive grain, Wear 269 (2010) 86–92.
[20] K. Lu, J. Lu, Nanostructured surface layer on metallic materials induced by surface mechanical attrition treatment, Mater. Sci. Eng. A 375–377 (2004) 38–45.
[21] M. Thomas, M. Jackson, The role of temperature and alloy chemistry on subsurface deformation mechanisms during shot peening of titanium alloys, Scr. Mater. 66 (2012) 1065–1068.
[22] M. Frija, T. Hassine, R. Fathallah, C. Bouraoui, A. Dogui, Finite element modelling of shot peening process: prediction of the compressive residual stresses, the plastic deformations and the surface integrity, Mater. Sci. Eng. A 426 (2006) 173–180.
[23] G.H. Majzoobi, R. Azizi, A. Alavi Nia, A three-dimensional simulation of shot peening process using multiple shot impacts, J. Mater. Process. Technol. 164 (165) (2005) 1226–1234.
[24] P. Sanjurjo, C. Rodriguez, I. Penuelas, T.E. Garcia, F.J. Belzunce, Influence of the target material constitutive model on the numerical simulation of a shot peening process, Surf. Coat. Technol. (2014) 822–831.
[25] H.Y. Miao, S. Larose, C. Perron, M. Levesque, On the potential applications of a 3d random finite element model for the simulation of shot peening, Adv. Eng. Softw. 40 (2009) 1023–1038.
[26] T. Kim, H. Lee, M. Kim, S. Jung, A 3d fe model for evaluation of peening residual stress under angled multi-shot impacts, Surf. Coat. Technol. (2012) 3981–3988.
[27] M. Korzynski, A model of smoothing slide ball-burnishing and an analysis of the parameter interaction, J. Mater. Process. Technol. (2009) 625–633.
[28] G. Kermouche, Scratch-based residual stress-field by scratch-based surface mechanical treatments (superfinishing, polishing, roller burnishing, in: J.M. Bergheau (Ed.), Modelisation and Simulation of Manufacturing Processes, Hermes, 2014, pp. 305–320.
[29] P. Balland, L. Tabourot, F. Degre, V. Moreau, An investigation of the mechanics of roller burnishing through finite element simulation and experiments, Int. J. Mach. Tools Manuf. (2013) 29–36.
[30] J. Rech, G. Kermouche, W. Grzesik, C. Garcia-Rosales, A. Khellouki, V. Garcia-Navas, Characterization and modelling of the residual stresses induced by belt finishing on AISI D2 52100 hardened steel, J. Mater. Process. Technol. 1 (3) (2008) 187–195.
[31] J. Kenda, G. Kermouche, F. Dumont, J. Rech, J. Kopac, Investigation of the surface integrity induced by abrasive flow machining on AISI D2 hardened steel, Int. J. Mater. Prod. Technol. 46 (2013) 19–31.

[32] P. Duranton, J. Devaux, V. Robin, P. Gilles, J.M. Bergheau, 3d modelling of multipass welding of a 316l stainless steel pipe, J. Mater. Process. Technol. 153 (154) (2004) 457–463.
[33] P. Heurtier, M.J. Jones, C. Desrayaud, J.H. Driver, F. Montheillet, D. Allehaux, Mechanical and thermal modelling of friction stir welding, J. Mater. Process. Technol. 171 (2006) 348–357.
[34] V.P. Kuznetsov, S.Y. Tarasov, A.I. Dmitriev, Nanostructuring burnishing and subsurface shear instability, J. Mater. Process. Technol. (2015) 327–335.
[35] E. Sauger, L. Ponsonnet, J.M. Martin, L. Vincent, Study of the tribologically transformed structure created during fretting tests, Tribol. Int. 33 (2000) 743–750.
[36] A.C. Sekkal, C. Langlade, A.B. Vannes, Tribologically transformed structure of titanium alloy (TiAl6V4) in surface fatigue induced by repeated impacts, Mater. Sci. Eng. A. 393 (2005) 140–146.
[37] M. Busquet, S. Descartes, Y. Berthier, Formation conditions of mechanically modified superficial structures for two steels, Tribol. Int. 42 (2009) 1730–1743.
[38] G. Kermouche, G. Pacquaut, C. Langlade, J.M. Bergheau, Investigation of mechanically attrited structures induced by repeated impacts on an AISI 1045 steel, C. R. Mecanique 339 (2011) 552–562.
[39] E. Demir, D. Raabe, N. Zaafarani, S. Zaefferer, Investigation of the indentation size effect through the measurement of the geometrically necessary dislocations beneath small indents of different depths suing EBSD tomography, Acta Mater. 57 (2009) 559–569.
[40] B. Devincre, L. Kubin, T. Hoc, Physical analyses of crystal plasticity by dd simulation, Scr. Mater. 54 (2006) 741–746.
[41] L. Kubin, B. Devincre, T. Hoc, Modeling dislocation storage rates and mean free paths in face-centered cubic crystals, Acta Mater. 56 (2008) 6040–6049.
[42] L. Kubin, T. Hoc, B. Devincre, Dynamic recovery and its orientation dependence in face-centered cubic crystals, Acta Mater. 57 (2009) 2567–2575.
[43] Y. Liu, S. Varghese, J. Ma, M. Yoshino, H. Lu, R. Komanduri, Orientation effects in nanoindentation of single crystal copper, Int. J. Plast. 24 (2008) 1990–2015.
[44] O. Casals, S. Forest, Finite element crystal plasticity analysis of spherical indentation in bulk single crystals and coatings, Comput. Mater. Sci. 45 (2009) 774–782.
[45] J. Alcala, D. Esque-de los Ojos, Extending the contact regimes to single-crystal indentations, C. R. Mecanique 339 (2011) 458–465.
[46] J. Alcala, D. Esque-de los Ojos, Toward the development of continuum single-crystal contact mechanics analyses to microindentation experiments, Comput. Mater. Sci. 52 (2012) 14–19.
[47] Y. Liu, A.H.W. Ngan, Depth dependence of hardness in copper single crystals measured by nanoindentation, Scr. Mater. 44 (2001) 337–341.
[48] Simulia, Abaqus explicit user's manual, Dassault Systèmes (2013).
[49] H.J. Chang, M. Fivel, D. Rodney, M. Verdier, Multiscale modelling of indentation in fcc metals: from atomic to continuum, C. R. Phys. (2010) 285–292.
[50] P. Franciosi, M. Berveiller, A. Zaoui, Latent hardening in copper and aluminium single crystals, Acta Metall. 28 (3) (1980) 273–283.
[51] R. Madec, B. Devincre, L. Kubin, T. Hoc, D. Rodney, The role of collinear interaction in dislocation-induced hardening, Science (2003) 1879–1882.
[52] J. Alcala, O. Casals, J. Ocenasek, Micromechanics of pyramidal indentation in fcc metals: single crystal plasticity finite element analysis, J. Mech. Phys. Solids 56 (2008) 3277–3303.
[53] T. Belytschko, W. Kam Liu, B. Moran, Non-linear Finite Elements for Continua and Structures, Wiley, 2000.
[54] T. Hoc, J. Crépin, L. Gelebart, A. Zaoui, A procedure for identifying the plastic behavior of single crystals from the local response of polycrystals, Acta Mater. (2003) 5477–5488.
[55] C. Maurice, J. Driver, R. Fortunier, On solving the orientation gradient dependency of high angular resolution EBSD, Ultramicroscopy 113 (2012) 171–181.